Monthly Notices
of the
ROYAL ASTRONOMICAL SOCIETY

MNRAS **475,** 321–330 (2018)
Advance Access publication 2017 December 9

doi:10.1093/mnras/stx3178

Correcting the extended-source calibration for the *Herschel*-SPIRE Fourier-transform spectrometer

I. Valtchanov,[1⋆] R. Hopwood,[1,2] G. Bendo,[3] C. Benson,[4] L. Conversi,[5] T. Fulton,[4,6] M. J. Griffin,[7⋆] T. Joubaud,[2] T. Lim,[1,8] N. Lu,[9] N. Marchili,[10] G. Makiwa,[4] R. A. Meyer,[2,11] D. A. Naylor,[4] C. North,[7] A. Papageorgiou,[7] C. Pearson,[8,12,13] E. T. Polehampton,[8] J. Scott,[4] B. Schulz,[14] L. D. Spencer,[4] M. H. D. van der Wiel[4,15] and R. Wu[16]

[1]*Telespazio Vega UK for ESA, European Space Astronomy Centre, Operations Department, E-28691 Villanueva de la Cañada, Spain*
[2]*Department of Physics, Imperial College London, Prince Consort Road, London SW7 2AZ, UK*
[3]*UK ALMA Regional Centre Node, Jodrell Bank Centre for Astrophysics, School of Physics and Astronomy, University of Manchester, Manchester M13 9PL, UK*
[4]*Department of Physics & Astronomy, Institute for Space Imaging Science, University of Lethbridge, 4401 University Drive, Lethbridge, AB T1K 3M4, Canada*
[5]*European Space Astronomy Centre (ESA/ESAC), Operations Department, E-28691 Villanueva de la Cañada, Spain*
[6]*Blue Sky Spectroscopy, Lethbridge, AB T1J 0N9, Canada*
[7]*School of Physics and Astronomy, Cardiff University, The Parade, Cardiff CF24 3AA, UK*
[8]*RAL Space, Rutherford Appleton Laboratory, Chilton, Didcot, Oxfordshire OX11 0QX, UK*
[9]*South American Center for Astronomy, CAS, Universidad de Chile, Camino El Observatorio 1515, Las Condes, Santiago, Chile*
[10]*IAPS-INAF, Via Fosso del Cavaliere 100, I-00133 Roma, Italy*
[11]*Institute of Physics, Laboratory of Astrophysics, Ecole Polytechnique Fédérale de Lausanne, CH-1015 Lausanne, Switzerland*
[12]*School of Physical Sciences, The Open University, Milton Keynes MK7 6AA, UK*
[13]*Oxford Astrophysics, Denys Wilkinson Building, University of Oxford, Keble Rd, Oxford OX1 3RH, UK*
[14]*Infrared Processing and Analysis Center, California Institute of Technology, MS 100-22, Pasadena, CA 91125, USA*
[15]*ASTRON, the Netherlands Institute for Radio Astronomy, Postbus 2, NL-7990 AA Dwingeloo, the Netherlands*
[16]*LERMA, Observatoire de Paris, PSL Research University, CNRS, Sorbonne Universités, UPMC Univ. Paris 06, F-92190 Meudon, France*

Accepted 2017 December 5. Received 2017 December 4; in original form 2017 August 30

ABSTRACT

We describe an update to the *Herschel*-Spectral and Photometric Imaging Receiver (SPIRE) Fourier-transform spectrometer (FTS) calibration for extended sources, which incorporates a correction for the frequency-dependent far-field feedhorn efficiency, $\eta_{\rm ff}$. This significant correction affects all FTS extended-source calibrated spectra in sparse or mapping mode, regardless of the spectral resolution. Line fluxes and continuum levels are underestimated by factors of 1.3–2 in thespectrometer long wavelength band (447–1018 GHz; 671–294 μm) and 1.4–1.5 in the spectrometer short wavelength band (944–1568 GHz; 318–191 μm). The correction was implemented in the FTS pipeline version 14.1 and has also been described in the SPIRE Handbook since 2017 February. Studies based on extended-source calibrated spectra produced prior to this pipeline version should be critically reconsidered using the current products available in the Herschel Science Archive. Once the extended-source calibrated spectra are corrected for $\eta_{\rm ff}$, the synthetic photometry and the broad-band intensities from SPIRE photometer maps agree within 2–4 per cent – similar levels to the comparison of point-source calibrated spectra and photometry from point-source calibrated maps. The two calibration schemes for the FTS are now self-consistent: the conversion between the corrected extended-source and point-source calibrated spectra can be achieved with the beam solid angle and a gain correction that accounts for the diffraction loss.

Key words: instrumentation: spectrographs – space vehicles: instruments – techniques: spectroscopic.

1 INTRODUCTION

The calibration of an instrument consists of two tasks: (i) removing all instrument signatures from the data and (ii) converting the

⋆ E-mail: Ivan.Valtchanov@sciops.esa.int (IV); Matt.Griffin@astro.cf.ac.uk (MJG)

products to physical units using a suitable calibration schema. For the first task, a good knowledge of the instrument and its response to different conditions (e.g. observing mode, internal and external thermal and radiation environments, the solar aspect angle, etc.) is required. For the second task, a calibration source of assumed flux or temperature is used to convert the measured signal to physically meaningful units. The atmosphere blocks most far-infrared radiation from reaching the ground, therefore the calibration of far-infrared space borne instrumentation requires a bootstrapping approach based on previous observations and theoretical models of candidate sources, typically planets or asteroids.

An imaging Fourier-transform spectrometer (FTS) is part of the Spectral and Photometric Imaging Receiver (SPIRE; Griffin et al. 2010) on board the *Herschel Space Observatory* (Pilbratt et al. 2010). SPIRE is one of the most rigorously calibrated far-infrared space instruments to date. It underwent five ground-based test campaigns and regular calibration observations during the nearly 4 yr of in-flight operations of *Herschel*. The stable space environment at the second Lagrange point and the flawless operation of the instrument resulted in unprecedented accuracy both in terms of the telescope and instrument response. A detailed description of the FTS instrument and its calibration scheme is provided in Swinyard et al. (2010), with an update in Swinyard et al. (2014).

There are no prior systematic studies of the extended-source calibration for the FTS. Extended-source calibrated maps from the SPIRE photometer, corrected to the absolute zero level derived via cross-calibration with *Planck*-HFI (Bertincourt et al. 2016), became available during the post-operations phase of *Herschel*. These maps allowed for a detailed comparison between photometry and spectroscopy of extended sources. Initial checks showed significant and systematic differences at levels of 40–60 per cent across the three photometer bands. Some authors also reported discrepancies (Kamenetzky et al. 2014; Köhler et al. 2014) and implemented corrections in order to match the spectra with the photometry. Others proceeded by starting from the point-source calibration and correcting for the source size (e.g. Kamenetzky et al. 2015; Wu et al. 2015; Makiwa et al. 2016; Morris et al. 2017; Schirm et al. 2017).

The reported differences with the photometer did not initially draw our attention, because the comparison is intricate and depends on the assumptions made. As shown in Wu et al. (2013), the coupling of sources that are neither point-like nor fully extended (i.e. semi-extended) require good knowledge of the FTS beam and its side-lobes, as well as good knowledge of the source brightness distribution. Even extended sources with significant sub-structure couple in a complicated way with the multimoded and non-Gaussian beam (Makiwa et al. 2013). Moreover, the source size would imply colour-correcting the photometry (see Valtchanov 2017, The SPIRE Handbook, section 5.8; H17 from now on). Hence, both sides of the comparison need their proper corrections.

In this study, we have tried to alleviate some of the uncertainties by carefully selecting truly extended sources for cross-comparison with broad-band intensities from the SPIRE photometer extended-source calibrated maps. The results of this analysis show a significant correction is needed in order to match the extended-source calibrated spectra with the photometry. This paper introduces the methods used to derive the necessary corrections, demonstrates the self-consistency between FTS point and extended-source calibrated spectra, and demonstrates a good agreement with broad-band photometry from the SPIRE photometer.

Herschel's two other instruments, the Heterodyne Instrument for the Far Infrared (HIFI; de Graauw et al. 2010) and the Photodetector Array Camera and Spectrometer (PACS, Poglitsch et al. 2010), share some spectral overlap with the SPIRE FTS. Analysis of a sample of calibration targets has shown an overall agreement of ±20 per cent between the SPIRE FTS and HIFI, and discrepancies up to a factor of 1.5–2 for comparisons with PACS (Puga et al., in preparation). Noting that the instantaneous bandwidth of HIFI (2.4 or 4 GHz depending on observing mode and band) is only marginally wider than the instrumental line shape of the SPIRE FTS (1.2 GHz), the overall agreement between HIFI and the SPIRE FTS is acceptable. The spectral overlap between the SPIRE FTS and the PACS spectrometer falls in 194–210 μm, which is an area affected by a PACS spectral leak (see Vandenbussche et al. 2016). Although we have performed a comparison between instruments for a sample of extended sources, some results were inconclusive and we have not included this work in this paper.

The structure of the paper is as follows. In Section 2 we briefly outline the extended-source calibration scheme. In Section 3 we compare FTS results with photometry from SPIRE maps using a selection of spatially extended sources and derive a correction that matches the known far-field feedhorn efficiency. In Section 4 we link the two FTS calibration schemes (i.e. the point-source and the corrected extended-source schemes) using the beam solid angle and a correction for diffraction loss. Some guidelines on using the corrected spectra are presented in Section 5. In Section 6 we outline the significance of the correction and the impact on deriving physical conditions if the uncorrected spectra are used. In Section 7 we present the conclusions.

As much as possible we follow the notations used in the SPIRE Handbook (H17). Throughout the paper we interchangeably use *intensity* and *surface brightness* as equivalent terms, in units of either (MJy sr^{-1}) or (W m^{-2} Hz^{-1} sr^{-1}).[1]

2 TELESCOPE MODEL BASED EXTENDED-SOURCE CALIBRATION

In the following, we briefly outline the main points in the FTS calibration scheme, which is presented in greater detail in Swinyard et al. (2014).

As there is no established absolute calibration source for extended emission in the far-infrared and sub-mm bands, the *Herschel* telescope itself is used as a primary calibrator for the FTS. The usual sources used from ground, such as the Moon and the big planets (e.g. Wilson, Rohlfs & Hüttemeister 2013), are either too close to the Sun/Earth or too bright for the instrument.

The SPIRE FTS simultaneously observes two very broad overlapping spectral bands. The signals are recorded with two arrays of hexagonally close-packed, feedhorn-coupled, bolometer detectors: the spectrometer short wavelength (SSW) array with 37 bolometers, covering 191–318 μm (1568–944 GHz) and the spectrometer long wavelength (SLW) array with 19 bolometers, covering 294–671 μm (1018–447 GHz). The bolometers operate at a temperature of ∼300 mK, which is achieved with a special ^{3}He sorption cooler (see H17 for more details).

Within the FTS, the radiation from the combination of the astronomical source, the telescope, and the instrument[2] is split into two

[1] 1 MJy sr^{-1} = 10^{-20} W m^{-2} Hz^{-1} sr^{-1}.

[2] The instrument contribution enters in the total radiation because of the Mach–Zehnder configuration of the FTS, where a second input port views an internal blackbody source (see H17 for more details).

beams. A moving mirror introduces an optical path difference between the two beams. The recombination of the beams produces an interferogram on each of the individual feedhorn-coupled bolometers. Hence, the recorded signal $V_{\rm obs}$ after Fourier transforming the interferograms, can be expressed as

$$V_{\rm obs}\left[{\rm V\,Hz^{-1}}\right] = R_{\rm S}I_{\rm S} + R_{\rm tel}M_{\rm tel} + R_{\rm inst}M_{\rm inst}, \quad (1)$$

where $I_{\rm S}$ is the source intensity, $M_{\rm tel}$ and $M_{\rm inst}$ are the intensities corresponding to the telescope and the instrument emission models. $R_{\rm S}$, $R_{\rm tel}$, and $R_{\rm inst}$ are the relative spectral response functions (RSRFs) of the system for the source, the telescope, and the instrument, respectively. We assume the instrument and telescope emissions to be fully extended in the beam, and well represented by blackbody functions and $R_{\rm S} = R_{\rm tel}$. The units of $I_{\rm S}$, $M_{\rm tel}$, and $M_{\rm inst}$ are [W m^{-2} Hz^{-1} sr^{-1}], therefore the RSRF are in units of [V Hz^{-1}/(W m^{-2} Hz^{-1} sr^{-1})].

The instrument is modelled as a single temperature blackbody, $M_{\rm inst} = B(\nu, T_{\rm inst})$, where $B(\nu, T)$ is the blackbody *Planck* function and $T_{\rm inst}$ is the temperature of the instrument enclosure in Kelvin (available from housekeeping telemetry). The instrument is usually at ∼5 K and following Wien's displacement law, the peak of the instrument emission is at ∼600 μm, thus $M_{\rm inst}$ is much more significant for the longer wavelength SLW band than for the SSW band.

The telescope model used in the pipeline is a sum of two blackbody models, one for the primary and one for the secondary mirrors:

$$M_{\rm tel} = E_{\rm corr}(t)\,\varepsilon_1\,(1-\varepsilon_2)\,B(\nu, T_{M1}) + \varepsilon_2\,B(\nu, T_{M2}), \quad (2)$$

where $\varepsilon_1 = \varepsilon_2 \equiv \varepsilon(\nu)$ is the frequency-dependent telescope mirror emissivity, and T_{M1} and T_{M2} are the average temperatures of the primary and secondary mirrors, obtained via telemetry from several thermometers placed at various locations on the mirrors. The emissivity in equation (2) was measured for representative mirror samples pre-launch by Fischer, Klaasen & Hovenier (2004). For a dusty mirror ε is of the order of 0.2–0.3 per cent in the 200–600 μm band, with large systematic uncertainties. The only measured point in the SPIRE band, at 496 μm, has $\varepsilon = 0.23^{+0.06}_{-0.12}$ per cent. Based on repeatability analysis of a number of 'dark sky' observations in Hopwood et al. (2014), the model was corrected by a small (sub 1 per cent) and mission-date dependent adjustment to the emissivity, $E_{\rm corr}(t)$.

During the *Herschel* mission around the second Lagrange point of the Earth–Sun system, the primary mirror temperature T_{M1} was of the order of 88 K and the secondary mirror T_{M2} was colder by 4–5 K, i.e. at around 84 K. Even with the low emissivity the telescope thermal emission is the dominant source of radiation recorded by the detectors. Only a few of the sky sources observed with the SPIRE spectrometer are brighter than $M_{\rm tel}$: nearby large planets (Mars, Saturn) and the Galactic Centre.

The calibration of the FTS requires the derivation of $R_{\rm tel}$, $R_{\rm inst}$, $M_{\rm tel}$, and $M_{\rm inst}$, as we can then recover the source intensity using

$$I_{\rm S}\left[{\rm W\,m^{-2}\,Hz^{-1}\,sr^{-1}}\right] = \frac{(V_{\rm obs} - R_{\rm inst}M_{\rm inst})}{R_{\rm tel}} - M_{\rm tel}. \quad (3)$$

Note that all quantities in equation (3) are frequency dependent and derived independently for each FTS band (see Fulton et al. 2014). As the two bands SSW and SLW overlap in 944–1018 GHz, the intensities in this region should match within the uncertainties.

The point-source calibration is built upon the extended-source calibration, using a suitable model of the emission of a point-like source. In the case of the SPIRE FTS, the primary calibrator is Uranus, which has an almost featureless spectrum in the FTS bands and a disc-averaged brightness temperature model known with uncertainties within ±3 per cent (ESA-4 model; Moreno 1998; Orton et al. 2014). The point-source conversion factor, $C_{\rm point}$, is derived as $C_{\rm point} = M_{\rm Uranus}/I_{\rm Uranus}$, where $I_{\rm Uranus}$ is the observed extended-source calibration intensity from the planet (following equation 3) and $M_{\rm Uranus}$ is the planet's model. $M_{\rm Uranus}$ is converted from the disc-averaged brightness temperature model in units of K to units of Jy, using the planet's solid angle, as seen from the *Herschel* telescope at a particular observing epoch (see H17 for details). Hence, $C_{\rm point}$ is in units of $\left[{\rm Jy}/\left({\rm W\,m^{-2}\,Hz^{-1}\,sr^{-1}}\right)\right]$. It is important to emphasize that as long as the model $M_{\rm Uranus}$ is a good representation of the planet's emission in the FTS bands, then the point-source calibration is invariant with respect to the extended-source calibration.

The point-source calibration was validated using Uranus and Neptune models, which showed an agreement within 3–5 per cent (Swinyard et al. 2014). Furthermore, the calibration accuracy was confirmed using a number of secondary calibrators (stars, asteroids) with the agreement at a level of 3–5 per cent between point-source calibrated spectra and the photometry from SPIRE point-source calibrated maps (Hopwood et al. 2015). Therefore, we consider the point-source calibration as well established and in this paper our focus is on the extended-source calibration.

3 CROSS-CALIBRATION WITH SPIRE PHOTOMETER

The SPIRE photometer and the FTS are calibrated independently and it is therefore important to cross-match measurements from observations of the same target. The cross-calibration can be considered as a critical validation of the different calibrations and whether their derived accuracies could be considered realistic. The cross-calibration in the case of point sources was already mentioned in the previous section, while in this section we restrict our discussion to the extended-source case.

The cross-calibration is performed between the extended-source calibrated spectra, obtained as described in Section 2, and the extended-source calibrated SPIRE photometer maps. These maps use detector timelines calibrated to the integrated signal of Neptune (Bendo et al. 2013) instead of the Neptune peak signal used for point-source calibrated maps. The arbitrary zero-level of each map is matched to the absolute zero level derived from *Planck* (Bertincourt et al. 2016). There is a good overlap of the SPIRE 350 μm band with the *Planck*-HFI 857 GHz band, and a relatively good overlap between the SPIRE 500 μm band and the *Planck*-HFI 545 GHz band. There is no *Planck* overlap for the SPIRE 250 μm band, so an extrapolation is used, based on a modified blackbody curve and the observed SPIRE 250 μm and *Planck*-HFI intensities (see H17 for more details). The overall uncertainty in the *Planck*-derived zero level is estimated at ∼10 per cent, but for maps that are comparable in size to the *Planck*-HFI beam (FWHM ≈5 arcmin, Planck Collaboration VII 2016) the uncertainty can be larger.

One of the most critical ingredients for extended-source calibration for any particular instrument is the knowledge of the beam and how the beam couples to a source (e.g. Ulich & Haas 1976; Wilson et al. 2013). Uncertainties on the beam solid angle or the beam profile as a function of frequency will lead to uncertainties in the derived quantities.

The SPIRE photometer beam maps were obtained using special observations of fine scans over Neptune and the same region of the sky at a different epoch when Neptune was no longer in the

field of view (i.e. the 'shadow' observation). Thanks to these two observations the photometer beams for the three bands have been characterized out to 700 arcsec and the beam solid angles are known down to the percentage level. Analysis of the beam maps for the three photometer bands indicates that the broad-band beams are unimodal and their cores are well modelled with 2D Gaussians (see H17; Schultz et al., in preparation).

On the other hand, the FTS beam was only measured out to a radial distance of 45 arcsec. The beam is multimoded and far from Gaussian, especially in the SLW band, which exhibits appreciable frequency-dependent beam FWHM variations (Makiwa et al. 2013). Hence, for sources with significant spatial brightness variation, the coupling with the beam is rather uncertain. Consequently, for the cross-calibration analysis, we need to identify spatially flat sources with as little source structure as possible within the FTS beam.

3.1 Selecting targets for cross-calibration

For all 1825 FTS observations performed with nominal bias mode (sparse and mapping modes, see H17), we extract an 11 × 11 pixel (66 arcsec × 66 arcsec) sub-image from the SPIRE 250 μm photometer map,[3] centred on the SSW central detector coordinates. The SPIRE 250 μm beam FWHM is 18 arcsec and the largest SPIRE FTS beam has a FWHM of 42 arcsec (Makiwa et al. 2013), so the selected sub-image is bigger than the largest FTS beam FWHM for all frequencies. To characterize the surface brightness distribution in each sub-image we introduce the relative variation $\sigma_{\rm I} = \sigma(I_{250})/\bar{I}_{250}$, where $\sigma(I_{250})$ is the standard deviation of the broad-band 250 μm brightness distribution in the region of interest and $\bar{I}_{250}$ is the average level. Because of the *Planck* zero level normalization $\bar{I}_{250} \gg 0$, no zero division effects are expected. To estimate the source flatness we extract the central row and column from the sub-image and calculate two arrays of ratios: North–South:East–West and North–South:West–East. While either ratio alone can identify a vertical or horizontal gradient, the two ratios are needed to detect sources with diagonal gradients. The measure of the maximum gradient $g_{\rm max}$ is the maximum value within the two ratio arrays, with $\Delta g_{\rm max} = |1 - g_{\rm max}|$. We empirically classify a source as flat if $\sigma_{\rm I} \leq 0.10$ and $\Delta g_{\rm max} \leq 0.2$.

Out of the 1825 FTS observations in nominal mode we identified 70 flat sources observed at high spectral resolution (HR).[4] Some are faint, which introduces a large scatter, especially at 500 μm; hence, we only consider those 53 flat HR-mode sources with $\bar{I}_{250} \geq 100$ MJy sr^{-1}.

Furthermore, all of these 53 sources have *Herschel* PACS photometer observations at 160 μm and either at 70 or 100 μm. We use the higher angular resolution PACS maps at 70 μm (or 100 μm), with the FWHM of the point-spread function of the order of 6–8 arcsec, to visually identify sources which are either point-like, semi-extended or have a significant sub-structure within a region of radius 1 arcmin. As a result of this visual check, we retain 24 out of the 53 sources as our final sample of flat sources. These sources are listed in Table 1, while Fig. 1 shows examples of 70 μm maps for two observations, a source from our selection (left) and a source that was rejected as having a complicated morphology (right).

[3] Very few FTS observations have no associated SPIRE photometer map.
[4] We do not include low resolution observations as in some cases the calibration introduces significant artefacts, mostly in the SLW band (Marchili et al. 2017).

3.2 Synthetic photometry from extended-source calibrated spectra

To derive synthetic photometry from a spectrum we follow the approach explained in H17 and in Griffin et al. (2013). The total RSRF-weighted in-beam flux density from a source with spectral energy distribution $I_{\rm S}(\nu)$ is

$$\bar{S}_{\rm S}\,[Jy] = \frac{\int_{\rm passband} I_{\rm S}(\nu)\eta(\nu)R(\nu)\Omega(\nu){\rm d}\nu}{\int_{\rm passband} \eta(\nu)R(\nu){\rm d}\nu}. \quad (4)$$

Here, $R(\nu)$ and $\eta(\nu)$ are the photometer spectral response function and the aperture efficiency for the passband. $\Omega(\nu)$ is the beam solid angle modelled with

$$\Omega(\nu) = \Omega(\nu_0)\left(\frac{\nu}{\nu_0}\right)^{2\gamma}, \quad (5)$$

where $\Omega(\nu_0)$ is the beam solid angle derived from Neptune and $\gamma = -0.85$, ν_0 is the adopted passband central frequency. The Neptune derived beam solid angles at the band centres (250, 350, 500) μm are $\Omega(\nu_0) = (469.35, 831.27, 1804.31)$ arcsec^2 (see H17).

A common convention in astronomy is to provide monochromatic flux densities or intensities at a particular central frequency ν_0, assuming a source with a power-law spectral shape: $I(\nu) \propto \nu^{-1}$. This convention is also used to calibrate the SPIRE photometer timelines. Hence, to convert $\bar{S}_{\rm S}$ to monochromatic intensity $I_{\rm S}(\nu_0)$ in [MJy sr^{-1}] for a source with $I(\nu) \propto \nu^{-1}$ we use

$$I_{\rm S}(\nu_0) = {\rm KMonE}(\nu_0) \times \bar{S}_{\rm S}, \quad (6)$$

where the conversion factors KMonE(ν_0) is

$${\rm KMonE}(\nu_0) = \frac{\nu_0^{-1}\int_{\rm passband} \eta(\nu)R(\nu){\rm d}\nu}{\int_{\rm passband} \nu^{-1}\eta(\nu)R(\nu)\Omega(\nu){\rm d}\nu}, \quad (7)$$

and the corresponding values are (91.567, 51.665, 23.711) in units of [MJy sr^{-1} per Jy/beam] for the three photometer bands at (250, 350, 500) μm.

We use equations (4) and (6) to derive the synthetic photometry of extended-source calibrated spectra $I_{\rm S}(\nu)$ from the two co-aligned central detectors of the two FTS bands. The error on the synthetic photometry is calculated by substituting $I_{\rm S}(\nu)$ in equation (4) with $I_{\rm S}(\nu) \pm \Delta I_{\rm S}(\nu)$, where $\Delta I_{\rm S}(\nu)$ is the standard error after averaging the different spectral scans in the pipeline (see Fulton et al. 2014 for details).[5]

The 250 and 500 μm photometer bands are fully covered by the SSW and SLW spectra; however, the 350 μm band is mostly in SLW but a small fraction falls within SSW (see Fig. 2). For a source with $I(\nu) \propto \nu^{-1}$, the underestimation of the synthetic photometry is ∼1 per cent and for a ν^2 spectrum it is overestimated by ∼2 per cent. These are within the overall calibration uncertainties and consequently we do not stitch together the SSW and SLW spectra before deriving the synthetic photometry at 350 μm.

3.3 Comparison with the photometer

For each of the 24 flat sources we derive synthetic photometry as described in Section 3.2. The resulting values can be directly

[5] This framework is implemented in the *Herschel* Interactive Processing Environment (HIPE) as a task `spireSynthPhotometry()`. The output of the task is the synthetic surface brightness values at 250, 350, and 500 μm in MJy sr^{-1}, for a monochromatic fully extended source with $I(\nu) \propto \nu^{-1}$.

Table 1. List of the final selection of spatially flat sources. The target name is that provided by the proposer. The equatorial coordinates RA and Dec. are for the central detector from the SSW array. For mapping we only used one FTS sparse snapshot out of 4 or 16 that were used to build the spectral cube. Only one SPIRE photometer and one PACS photometer OBSID are provided, although there can be multiple overlapping observations. If PACS and SPIRE photometer OBSIDs are the same then the observation was taken in Parallel Mode (see H17).

ID	Target	RA J2000 (deg)	Dec. J2000 (deg)	FTS ObsID	Obs mode	SPIRE Phot ObsID	PACS Phot ObsID
1	s104off	304.54185	36.77219	1342188192	Sparse	1342244191	1342244191
2	rcw120rhII	258.10234	−38.45376	1342191230	Sparse	1342204101	1342216586
3	rcw120off	258.25602	−38.45335	1342191233	Sparse	1342204101	1342216586
4	Cas A FTS Centre-1	350.87116	58.81551	1342202265	Sparse	1342188182	1342188207
5	rho_oph_fts_off	246.45504	−24.33656	1342204893	Mapping	1342205094	1342238817
6	rho_oph_fts_off_2	246.43947	−24.35357	1342204894	Mapping	1342205094	1342238817
7	EL29_int	246.81833	−24.58734	1342204896	Sparse	1342205094	1342238817
8	rcw82off2	209.74421	−61.33031	1342204901	Sparse	1342203279	1342203279
9	rcw82pdr	209.75750	−61.42321	1342204902	Sparse	1342203279	1342203279
10	rcw82rhII	209.86946	−61.38302	1342204904	Sparse	1342203279	1342203279
11	rcw82off	210.05859	−61.41489	1342204910	Sparse	1342203279	1342203279
12	rcw79rHII	205.09185	−61.74105	1342204913	Sparse	1342203086	1342258817
13	rcw79off	205.37508	−61.77444	1342204917	Sparse	1342203086	1342258817
14	n2023_fts_2	85.40126	−2.22890	1342204922	Mapping	1342215985	1342228914
15	02532+6028	44.30356	60.67048	1342204928	Sparse	1342226655	1342226620
16	IRAx04191_int	65.51420	15.48075	1342214851	Sparse	1342190615	1342241875
17	los_30+3	278.85175	−1.23758	1342216894	Sparse	1342206696	1342228961
18	los_28.6+0.83	280.13751	−3.48752	1342216895	Sparse	1342218695	1342218695
19	los_26.46+0.09	279.81675	−5.71094	1342216897	Sparse	1342218697	1342218697
20	PN Mz 3 OFF	244.28579	−52.03330	1342251316	Sparse	1342204046	1342204047
21	CTB37A-N ref	258.24149	−37.84571	1342251320	Sparse	1342214511	1342214511
22	G349.7 ref	259.06902	−37.19761	1342251324	Sparse	1342214511	1342214511
23	G357.7 ref	264.50619	−30.01860	1342251327	Sparse	1342204367	1342204367
24	G357.7B-IRS	264.61196	−30.57159	1342251328	Mapping	1342204367	1342204369

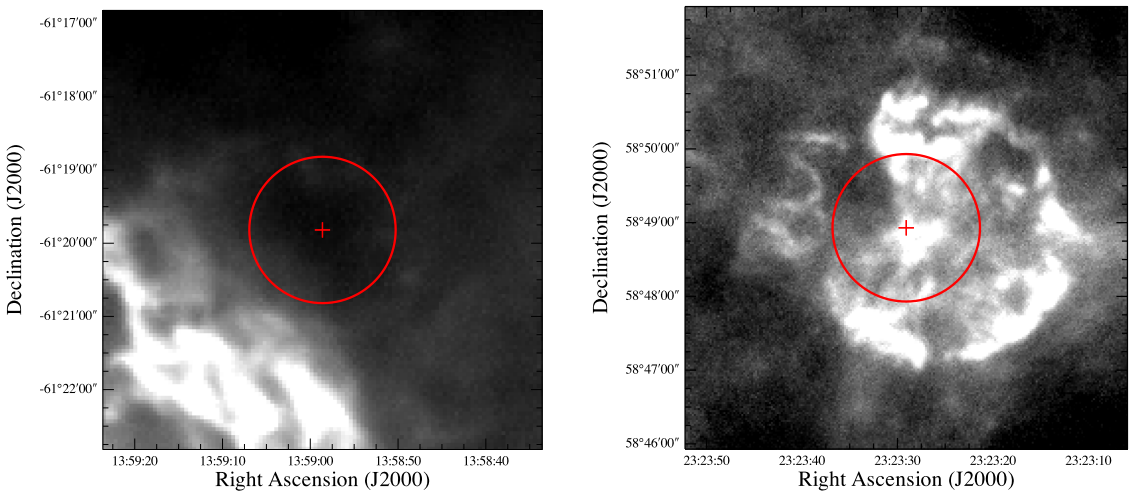

Figure 1. (Left) Spatially flat extended source, rcw82off2 (see Table 1), with grey-scale image corresponding to the PACS 70 μm map and the 1 arcmin radius unvignetted FTS field of view shown as a red circle. The centre of the FTS field is marked with a '+' sign. Note that the region appears as dark due to the very bright nearby rcw82; the peak surface brightness within the FTS footprint at 250 μm is more than 400 MJy sr^{-1}. (Right) Cas A – a supernova remnant shown with 70 μm PACS data that was rejected because of its complex morphology although $\Delta g_{\max} = 0.07$ and $\sigma_{\rm I} = 0.07$.

compared to the corresponding extended-source calibrated photometer maps, by using a suitable aperture to take the average surface brightness. We use a square box aperture of 30 arcsec, which differs from the one used for the selection of extended and flat sources (Section 3.1). However, since we are averaging the surface brightness of flat extended sources then the choice of aperture is not important, as long as the size is comparable with the FTS beam.

Fig. 2 shows the extended-source calibrated spectrum produced with version 13.1 of the FTS pipeline[6] for one of the flat sources (rcw82off2, ID8 in Table 1) and the derived synthetic photometry compared with the average surface brightness on

[6] Version 13.1 of the pipeline is the last one before the correction described in this paper was implemented.

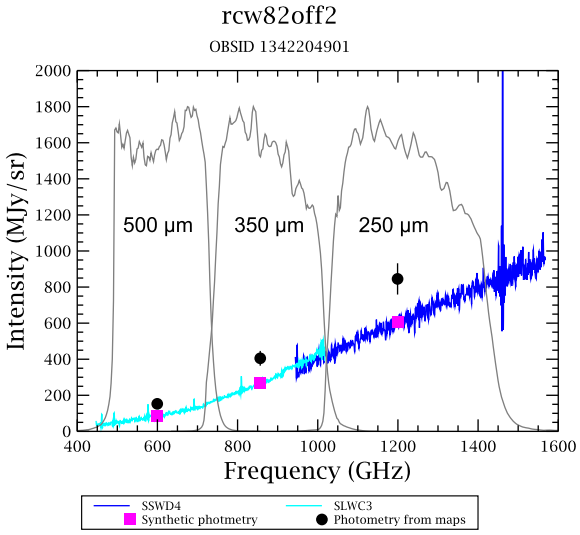

Figure 2. Comparison of the synthetic photometry from the extended-source calibrated spectra from version 13.1 of the pipeline and the surface brightness from photometer maps. The same source, rcw82off2, as in Fig. 1 is shown. The spectra are shown in blue for SSW and in cyan for SLW. The derived synthetic photometry points at the three photometer bands are shown as filled magenta squares. The error bars are smaller than the symbols and they include the errors from the scan-averaged spectra (see Fulton et al. 2014). The photometer RSRFs are shown in grey, each one annotated with the band central wavelength. The average surface brightness values from photometer maps are shown as filled black circles. The error bars for the photometer points include the 10 per cent *Planck*-to-SPIRE zero offset uncertainty and the standard deviation of the brightness distribution in the selected box.

photometer maps within the 30 arcsec box aperture. It is obvious that there is a significant offset between the synthetic photometry and the measured photometry in maps, with ratios of phot/spec ($1.38 \pm 0.10, 1.50 \pm 0.06, 1.77 \pm 0.20$) at (250, 350, 500) μm for this particular target.

The combined results for the averaged spec/phot ratio for each band for all 24 flat sources are shown as blue squares in Fig. 3. The errors bars for each point include the standard deviation of the aperture photometry, the 10 per cent uncertainty from the *Planck* zero level offset and the error from the synthetic photometry. This figure unequivocally demonstrates that there is a systematic and significant discrepancy between the FTS and photometer extended-source calibrations.

3.4 The far-field feedhorn efficiency

The results shown in Fig. 3 (as well as the example in Fig. 2) indicate that in order to match the spectra with the photometry from extended-source calibrated maps we need to apply a correction. We consider the SPIRE photometer extended-source calibration more straight forward than that of the spectrometer: simple beam profile, unimodal Gaussian beam and the beam solid angle is known down to <1 per cent uncertainty, and is consequently much more representative and robust. Moreover, the photometer maps are cross-calibrated with *Planck*-HFI. Therefore, the correction should be applied to the SPIRE FTS extended-source calibrated spectra.

The derived ratios, shown in Fig. 3, are a good match to the far-field feedhorn efficiency curve, $\eta_{\rm ff}$. The correction, $\eta_{\rm ff}$ was introduced in empirical form in Wu et al. (2013), where it was linked with two other corrections: the diffraction loss predicted by the

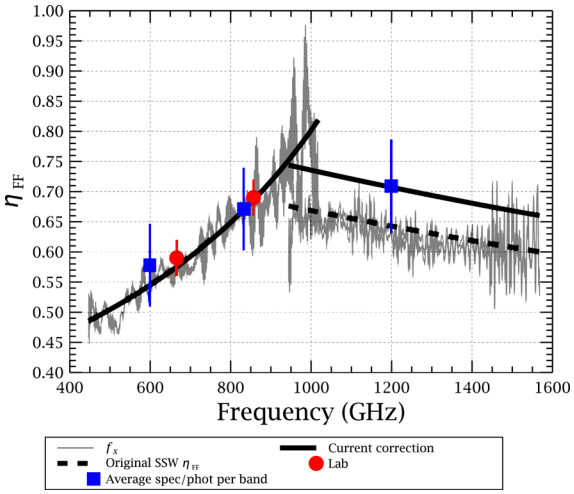

Figure 3. Averaged ratios of the synthetic photometry versus the results from photometer maps for all 24 flat sources (filled blue squares), together with the far-field feedhorn efficiency (black lines, see equation 8) and the laboratory measurements from Chattopadhyay et al. (2003) (filled red circles). The dashed line is the original $\eta_{\rm ff}$ for SSW as presented in Wu et al. (2013). The grey curves are the ratios $f_X = \eta_{\rm diff}\, I_{\rm S}\, \Omega_{\rm beam}/S_{\rm S}$ for all of the 24 flat sources (see Section 4).

optics model, $\eta_{\rm diff}$ (Caldwell et al. 2000) and the correction efficiency $\eta_{\rm c}$, with $\eta_{\rm ff} = \eta_{\rm c}/\eta_{\rm diff}$. As discussed in Wu et al. (2013), for point-like sources $\eta_{\rm c} \approx 1$, while for extended sources $\eta_{\rm c} \ll 1$ with the difference attributed to a combination of diffraction losses ($\eta_{\rm diff}$) and different response of the feedhorns and bolometers to a source filling the aperture and to that of a point source.

The far-field feedhorn efficiency $\eta_{\rm ff}$ was measured by Chattopadhyay et al. (2003) but only for the SLW band (the two laboratory measurements are shown as red circles in Fig. 3). The empirical $\eta_{\rm ff}$ from Wu et al. (2013) is 10 per cent lower for SSW (shown as a dashed line in Fig. 3) with respect to the measured ratio at 250 μm. This 10 per cent is within the uncertainty of the 250 μm average ratio, however, the original empirical $\eta_{\rm ff}$ would introduce a significant discontinuity in the overlap region of the two FTS bands (944–1018 GHz). In order to avoid this inconsistency, $\eta_{\rm ff}$ was rescaled by 10 per cent for SSW, so that it matches the 250 μm ratio and also avoids the discontinuity. It is irrelevant to attribute this 10 per cent offset to any parameter in the optical model ($\eta_{\rm diff}$; Caldwell et al. 2000). The most likely interpretation is that some unknown effects in the complicated feedhorn-coupled system lead to a different response for fully extended sources only for SSW, which leads to $\eta_{\rm c} = 1.1$ for SSW, while for SLW $\eta_{\rm c} = 1$.

In practice, due to implementation considerations, we use the following empirical approximation based on the $\eta_{\rm ff}$ curves shown in fig. 4 in Wu et al. (2013), with SSW rescaled by 10 per cent:

$$\begin{aligned} &\text{SLW}: 1/\eta_{\rm ff} = 2.7172 - 1.47 \times 10^{-3}\nu, \\ &\text{SSW}: 1/\eta_{\rm ff} = 1.0857 + 2.737 \times 10^{-4}\nu, \end{aligned} \quad (8)$$

where ν is the frequency in GHz. The two curves are shown in Fig. 3. And the corrected intensities are

$$I'_{\rm ext} = I_{\rm ext}/\eta_{\rm ff}, \quad (9)$$

where $I_{\rm ext}$ is the extended-source calibrated spectrum from Swinyard et al. (2014) calibration [see also equation (3)]. Performing the same comparison for $I'_{\rm ext}$ with the extended-calibrated maps from the photometer for the 24 flat sources, we obtain the ratios as shown in Fig. 4. On average we see a good agreement at a level of 2–4

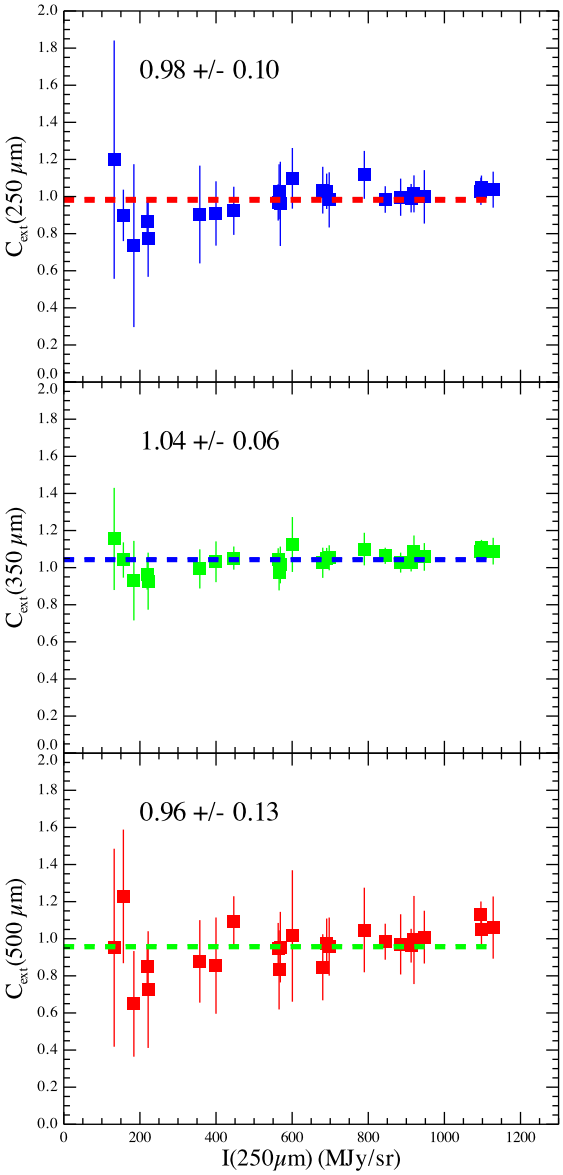

Figure 4. $C_{\rm ext}(\nu_0) = I_{\rm phot}(\nu_0)/I_{\rm spec}(\nu_0)$ as a function of $\bar{I}_{250\,\mu\rm m}$ at 250 μm (top), at 350 μm (middle), and 500 μm (bottom) for the 24 flat sources. The mean (shown as a dashed line) and the standard deviation for each band are annotated in each panel: from top to bottom, 250, 350, and 500 μm.

per cent, comparable to that found for the point-source calibration in Hopwood et al. (2015).

4 CONVERTING TO POINT-SOURCE CALIBRATION

For an extended source on the sky $I_{\rm S}(\theta, \phi)$, the measured flux density is

$$S_{\rm S}(\nu) = \eta \oint_{4\pi} P(\theta, \phi)\, I_{\rm S}(\theta, \phi) {\rm d}\Omega, \qquad (10)$$

where $P(\theta, \phi)$ is the normalized beam profile and η represents all angle-independent efficiency factors that affect the system gain. The integration is over a region subtended by the source.

For a spatially flat source, $I(\theta, \phi) = I_{\rm S}(\nu) =$ constant, and assuming that the source is much more extended than the beam, we can write

$$S_{\rm S}(\nu) = \eta \times I_{\rm S}(\nu) \times \Omega_{\rm beam}(\nu), \qquad (11)$$

where $\Omega_{\rm beam}(\nu) = \oint_{4\pi} P(\theta, \phi){\rm d}\Omega$ is the main beam solid angle.

Equation (11) should be valid for any instrument. And it is indeed the case for the SPIRE photometer, where the conversion from point-source to extended-source calibrated maps can be achieved by multiplication with $K_{\rm PtoE}(\nu) \equiv \Omega_{\rm pip}$, where $\Omega_{\rm pip}$ is the beam solid angle used in the data processing pipeline (see H17 for more details). The gain and aperture corrections already incorporated in the point-source calibrated timelines in the data processing pipeline.

The validity of equation (11) for the corrected extended-source calibrated spectra is demonstrated in Fig. 5 for a point source (Neptune) and an extended source from the sample of 24 spatially flat sources. In this case, the efficiency factor η is actually the diffraction loss correction, $\eta_{\rm diff}$ as derived by Caldwell et al. (2000), using a simple optics model, incorporating the telescope secondary mirror and mirrors support structures. For a point source on axis $\eta_{\rm diff}$ is of the order of 75 per cent. We see that equation (11) is fulfilled at a level of ±5 per cent, if we exclude noisier regions close to the band edges (Fig. 5, bottom panels).

The noise that appears in the point-source converted spectra in Fig. 5 (cyan curves) reflects the small-scale characteristics of $R_{\rm tel}$ that are inherently present in $I'_{\rm ext}$. The original point-source calibrated spectrum of Neptune (Fig. 5, left) has much less noise because the point-source calibration is based on the smooth featureless model spectrum of Uranus and consequently $C_{\rm point}$ accounts for those small-scale features of $R_{\rm tel}$. Therefore, the pipeline-provided point-source calibrated spectra are better products and they should be used, rather than converting the extended-source calibration with equation (11).

Interestingly, the missing correction for the old calibration of the FTS extended-source spectra is obvious, if we construct the ratio of the left-hand and right-hand side of equation (11), i.e. $f_X = \eta_{\rm diff}\, I_{\rm S}\, \Omega_{\rm beam}/S_{\rm S}$. This ratio should be 1 if equation (11) is valid, but as shown in Fig. 3, the grey curves, which are the derived f_X for all 24 flat sources with the old calibration, match well with the empirical $\eta_{\rm ff}$ instead.

5 PRACTICAL CONSIDERATIONS

All extended-source calibrated spectra, regardless of the observing mode and the spectral resolution, are corrected for the missing far-field feedhorn efficiency (equation 9). Using those for analysis of extended sources is straightforward: measuring lines and the continuum, with results in the corresponding units of W m^{-2} sr^{-1}. A large fraction of the sources observed with the FTS, however, are neither point-like nor fully extended, we call them semi-extended sources. The framework for correcting the spectra for this class of targets is presented in Wu et al. (2013) and implemented in HIPE as an interactive tool – the SEMIEXTENDEDCORRECTOR (SECT). There are two possible ways to derive a correction for the source size (and/or a possible pointing offset): starting from an extended-source or from a point-source calibrated spectrum (see Wu et al. 2013, equation 14). The SECT implementation in HIPE follows the procedure starting from a point-source calibrated spectrum. As the point-source calibration is not affected by the far-field feedhorn efficiency correction, described in Section 3.4, so there should not be any changes in the SECT-corrected spectra.

In cases when there is a point source embedded in extended emission, then the background subtraction should be performed using the point-source calibrated spectra, regardless of the fact that

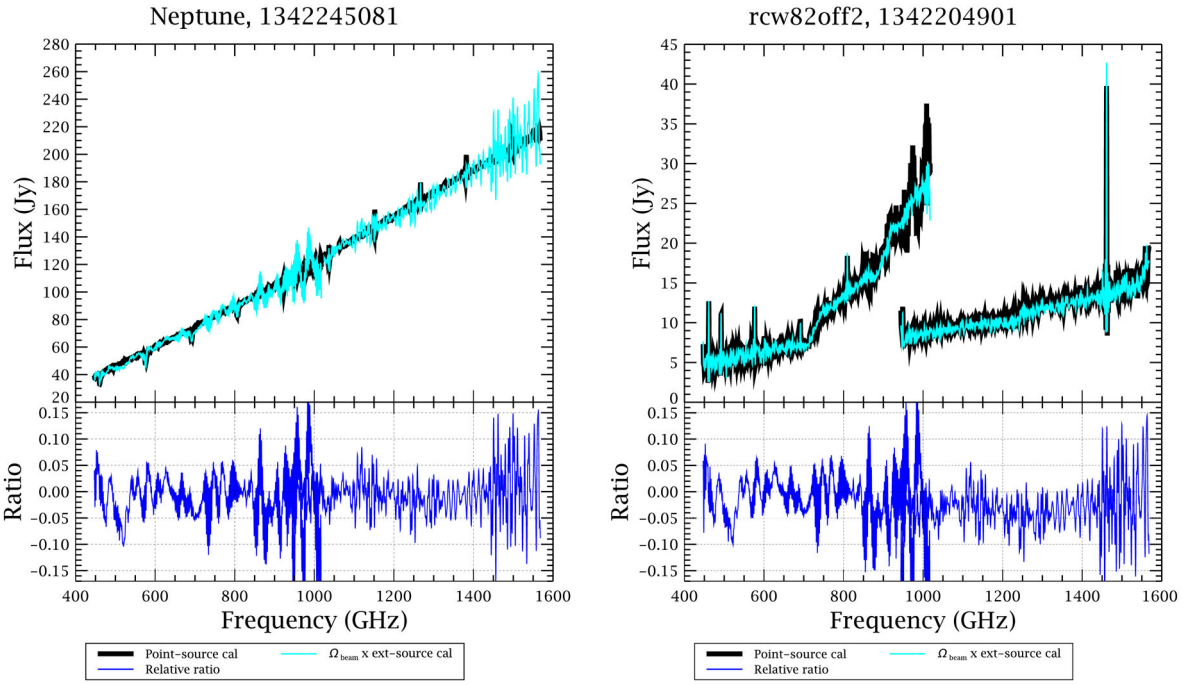

Figure 5. Left-hand panel: comparison of Neptune pipeline derived point-source calibrated flux density $S_S(\nu)$ in Jy (thick black line) with the flux density derived from the extended-source calibrated intensity $S'_S = \eta_{diff} \times I'_S(\nu) \times \Omega_{beam}$ (cyan), i.e. equation (11). The relative ratio of S'_S/S_S is shown in the bottom panel. The overall agreement, in the less noisy parts of the two bands, is within 5 per cent. Right-hand panel: the same comparison for a fully extended source.

the background may be fully extended in the beam. If you perform the background subtraction using I'_{ext}, then you cannot any longer use C_{point} to convert the background subtracted spectrum to a point-source calibrated one. Instead, you have to use equation (11), and as explained in Section 4, this will introduce unnecessary noise in the final spectrum.

The same consideration is applicable for semi-extended sources, where the first step before the correction should be the background subtraction and then proceeding with SECT, both steps should be performed on point-source calibrated spectra.

Careful assessment of the source extension is always necessary, because in some cases the source may fall in the extended-source category in continuum emission but semi-extended or point-like in a particular line transition. This will dictate which calibration to use and what corrections to apply to the line flux measurements.

Finally, if for some reason one needs to recover the spectrum with the original calibration following Swinyard et al. (2014), then C_{point}[7] and the point-source calibrated spectrum can be used: $I_{ext} = S_S/C_{point}$.

6 IMPLICATIONS FOR SPIRE FTS USERS AND ALREADY PUBLISHED RESULTS

The significant correction for the extended-source calibration scheme presented by this work, was implemented as of HIPE version 14.1, and has already been described in H17 since 2017 February. All analysis based on extended-source calibrated FTS spectra, produced prior to that version, will be affected by the significant and systematic shortfall of the old calibration. Any integrated line intensity or continuum measurements will be underestimated by a factor of 1.3–2 and using them to derive physical conditions in objects will be subject to corresponding systematic errors.

[7] C_{point} is available as a calibration table within the SPIRE calibration context (see H17 and Appendix).

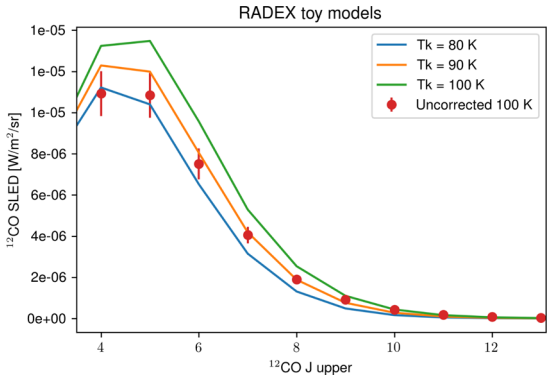

Figure 6. ^{12}CO spectral line energy distribution model from RADEX (van der Tak et al. 2007) for an emitting region, assuming $n(H_2) = 6.3 \times 10^3$ cm^{-3}, column density of 10^{16} cm^{-2}, and kinetic temperatures of 100 K (green curve), 90 K (orange), and 80 K (blue). The 100 K SLED is multiplied by η_{ff} and the new uncorrected SLED is shown with red points with error bars assuming a conservative 10 per cent uncertainty in line flux measurements.

To illustrate the magnitude of the deviations on the derived physical characteristics with the old calibration, we performed a simple simulation using RADEX (van der Tak et al. 2007). We modelled the spectral line energy distribution (SLED) of the ^{12}CO lines from an emitting region with molecular hydrogen density $n(H_2) = 6.3 \times 10^3$ cm^{-3}, column density of 10^{16} cm^{-2}, and kinetic temperatures T_{kin} of 100, 90, and 80 K. The predicted line fluxes for the three temperatures in the SPIRE FTS bands are shown in Fig. 6 as green, orange, and blue curves, respectively.

If we observe a region with $T_{kin} = 100$ K, but we use the old calibration, then the measured ^{12}CO lines (the green curve) will

be underestimated by a factor of $\eta_{\rm ff}$; these are shown in Fig. 6 as red points with 10 per cent measurement errors. Obviously the red points do not match the RADEX models with $T_{\rm kin} = 100$ K, they are at least 2–3 σ away from the correct input model for lines with upper J ≤ 8. While models with $T_{\rm kin}$ between 85 and 90 K are much closer to the 'measurements' and consequently the derived temperature from the red points will be significantly underestimated.

Using the old calibration for studies based on line-to-line or line-to-continuum measurement will not be significantly biased for SSW, because the variation of $\eta_{\rm ff}$ with frequency within the band is small. However, the variation across SLW is significant and in this case using uncorrected data will lead to the incorrect results.

The $\eta_{\rm ff}$ correction to extended-source calibrated spectra results in new values for the frequency-dependent additive continuum offsets and FTS sensitivity estimates (see Hopwood et al. 2015). The new offsets and sensitivities are presented in H17 and their tabulation is available in the *Herschel* legacy repository as Ancillary Data Products.[8]

The correction with $\eta_{\rm ff}$ also introduces a new source of uncertainty to the overall calibration error budget for extended sources. The two measurement points for $\eta_{\rm ff}$ in SLW band have errors of 3 per cent (Chattopadhyay et al. 2003), and we assume the same error is applicable for the SSW band. Therefore, the overall calibration accuracy budget for extended-source calibration will have to incorporate the 3 per cent statistical uncertainty on $\eta_{\rm ff}$. As the correction is semi-empirical and based on cross-calibration with the SPIRE photometer, the more conservative estimate of the overall uncertainty is of the order of 10 per cent, to match the uncertainties on the derived photometry ratios (Fig. 4).

7 CONCLUSIONS

We introduce a correction to the SPIRE FTS calibration for the far-field feedhorn efficiency, $\eta_{\rm ff}$. This brings the cross-calibration between extended-source calibrated data for the spectrometer and photometer in agreement at a 2–4 per cent level for fully extended and spatially flat sources. With this correction, the FTS point-source and extended-source calibration schemes are now self-consistent and can be linked together using the beam solid angle and a gain correction for the diffraction losses.

All SPIRE FTS extended-source calibrated products (spectra or spectral maps) in the *Herschel* Science Archive, processed with pipeline version 14.1 have already been corrected for $\eta_{\rm ff}$. Spectra processed with earlier versions are significantly underestimated and consequently the results derived with the old calibration should be critically revised. It is important to note that while the correction is close to a constant factor for the SSW band, this is not the case for SLW. Hence, even relative line-to-line or line-to-continuum analysis for SLW is affected.

We have not discussed any possible reason as to why the far-field feedhorn efficiency was not naturally incorporated in the extended-source calibration scheme. With *Herschel* no longer operational, it is not possible to take new measurements in order to check any hypothesis. We can only speculate about possible causes. One plausible reason is that the FTS beam, which was only measured out to a radial distance of 45 arcsec, compared to the 700 arcsec for the photometer, has an important fraction of the power distributed at larger distances, or in the side-lobes. Another possibility could be that the coupling of the two instruments to extended sources, viewed through the telescope, differs in an unknown manner such as small residual misalignment. Both these hypotheses could play a part in $\eta_{\rm ff}$ not being naturally incorporated into then extended-source calibration. The bottom line, however, is that with this correction the FTS calibration is now self-consistent and the cross-calibration with the SPIRE photometer is in good agreement.

Ground-based measurements of lines or continuum, in frequency ranges that overlap with the large spectral coverage of the FTS, may provide further insights on the correctness of the extended-source calibration, although the direct comparison will not be straight forward due to the complications in observing very extended emission with ground-based telescopes.

[8] See Appendix with a list of URLs for the data products.

ACKNOWLEDGEMENTS

The authors wish to thank the referee for their useful comments that helped improve the paper, as well as J. Kamenetzky, C. Wilson, D. Teyssier, K. Rygl, E. Puga, and K. Exter for valuable discussions.

SPIRE has been developed by a consortium of institutes led by Cardiff Univ. (UK) and including: Univ. Lethbridge (Canada); NAOC (China); CEA, LAM (France); IFSI, Univ. Padua (Italy); IAC (Spain); Stockholm Observatory (Sweden); Imperial College London, RAL, UCL-MSSL, UKATC, Univ. Sussex (UK); and Caltech, JPL, NHSC, Univ. Colorado (USA). This development has been supported by national funding agencies: CSA (Canada); NAOC (China); CEA, CNES, CNRS (France); ASI (Italy); MCINN (Spain); SNSB (Sweden); STFC, UKSA (UK); and NASA (USA). This research is supported in part by the Canadian Space Agency (CSA) and the Natural Sciences and Engineering Research Council of Canada (NSERC).

Most of the data processing and analysis in this paper was performed in the *Herschel* Interactive Processing Environment (HIPE, Ott 2010).

Herschel is an ESA space observatory with science instruments provided by European-led Principal Investigator consortia and with important participation from NASA.

REFERENCES

Bendo G. J. et al., 2013, MNRAS, 433, 3062
Bertincourt B. et al., 2016, A&A, 588, A107
Caldwell M., Swinyard B., Richards A., Dohlen K., 2000, Proc. SPIE, 4013, 210
Chattopadhyay G., Glenn J., Bock J., Rownd B., Caldwell M., Griffin M., 2003, IEEE Trans. Microw. Theory Tech., 51, 2139
de Graauw T. et al., 2010, A&A, 518, L6
Fischer J., Klaasen T., Hovenier N., 2004, Appl. Opt., 43, 3765
Fulton T. et al., 2014, Exp. Astron., 37, 381
Griffin M. J. et al., 2010, A&A, 518, L3
Griffin M. J. et al., 2013, MNRAS, 434, 992
Hopwood R. et al., 2014, Exp. Astron., 37, 195
Hopwood R. et al., 2015, MNRAS, 449, 2274
Kamenetzky J., Rangwala N., Glenn J., Maloney P. R., Conley A., 2014, ApJ, 795, 174
Kamenetzky J. et al., 2015, Highlights Astron., 16, 618
Köhler M. et al., 2014, A&A, 569, A109
Makiwa G., Naylor D. A., Ferlet M., Salji C., Swinyard B., Polehampton E., van der Wiel M. H. D., 2013, Appl. Opt., 52, 3864
Makiwa G., Naylor D. A., van der Wiel M. H. D., Ward-Thompson D., Kirk J. M., Eyres S., Abergel A., Köhler M., 2016, MNRAS, 458, 2150
Marchili N. et al., 2017, MNRAS, 464, 3331
Moreno R., 1998, PhD thesis, Univ. Paris, updated 2010 models are available at ESA Herschel Science Centre

Morris P. W., Gull T. R., Hillier D. J., Barlow M. J., Royer P., Nielsen K., Black J., Swinyard B., 2017, ApJ, 842, 79
Orton G. S. et al., 2014, Icarus, 243, 494
Ott S., 2010, in Mizumoto Y., Morita K.-I., Ohishi M., eds, ASP Conf. Ser. Vol. 434, Astronomical Data Analysis Software and Systems XIX. Astron. Soc. Pac., San Francisco, p. 139
Pilbratt G. L. et al., 2010, A&A, 518, L1
Planck Collaboration VII, 2016, A&A, 594, A7
Poglitsch A. et al., 2010, A&A, 518, L2
Schirm M. R. P. et al., 2017, MNRAS, 470, 4989
Swinyard B. M. et al., 2010, A&A, 518, L4
Swinyard B. M. et al., 2014, MNRAS, 440, 3658
Ulich B. L., Haas R. W., 1976, ApJS, 30, 247
Valtchanov I. (Ed.) 2017, The SPIRE Handbook, Herschel Science Centre, HERSCHEL-HSC-DOC-0798, v3.1 (H17)
van der Tak F. F. S., Black J. H., Schöier F. L., Jansen D. J., van Dishoeck E. F., 2007, A&A, 468, 627
Vandenbussche B. et al., 2016, PICC-KL-TN-041
Wilson T. L., Rohlfs K., Hüttemeister S., 2013, Tools of Radio Astronomy. Springer-Verlag Berlin, Heidelberg, doi:10.1007/978-3-642-39950-3
Wu R. et al., 2013, A&A, 556, A116
Wu R. et al., 2015, A&A, 575, A88

APPENDIX: AVAILABLE DATA PRODUCTS

Many useful calibration tables are available in the *Herschel* Legacy Area at http://archives.esac.esa.int/hsa/legacy. Here, we only list those with relevance to the current paper.

(i) **Planetary models**:
Models for the primary calibrators (Uranus and Neptune) are available at http://archives.esac.esa.int/hsa/legacy/ADP/PlanetaryModels/

(ii) **FTS sensitivity curves and additive continuum offsets**:
The curves derived from the updated calibration are available at http://archives.esac.esa.int/hsa/legacy/ADP/SPIRE/SPIRE-S_sensitivity_offset/

(iii) **Diffraction loss curves**:
The correction $\eta_{\rm diff}$ as presented in Wu et al. (2013), and based on the optics model from Caldwell et al. (2000) is available at http://archives.esac.esa.int/hsa/legacy/ADP/SPIRE/SPIRE_Diffraction_loss/

(iv) **SPIRE photometer RSRFs**:
The RSTFs $R(\nu)$ and the aperture efficiencies $\eta(\nu)$ are available at http://archives.esac.esa.int/hsa/legacy/ADP/SPIRE/SPIRE-P_filter_curves/

(v) **SPIRE calibration tree**:
The last one (SPIRE_CAL_14_3) as well as previous version of the calibration tables are available as Java archive files (jar) at http://archives.esac.esa.int/hsa/legacy/cal/SPIRE/user/

This paper has been typeset from a TEX/LATEX file prepared by the author.